Journal of Molecular Graphics and Modelling 41 (2013) 55–60

Contents lists available at SciVerse ScienceDirect

Journal of Molecular Graphics and Modelling

journal homepage: www.elsevier.com/locate/JMGM

Structural basis of femtomolar inhibitors for acetylcholinesterase subtype selectivity: Insights from computational simulations

Xiao-Lei Zhu, Ning-Xi Yu, Ge-Fei Hao, Wen-Chao Yang, Guang-Fu Yang*

Key Laboratory of Pesticide & Chemical Biology, College of Chemistry, Ministry of Education, Central China Normal University, Wuhan 430079, PR China

ARTICLE INFO

Article history:
Accepted 17 January 2013
Available online 4 February 2013

Keywords:
Acetylcholinesterase
Selectivity
Molecular dynamics
MM/PBSA π–π interaction

ABSTRACT

Acetylcholinesterase (AChE) is a key enzyme of the cholinergic nervous system. More than one gene encodes the synaptic AChE target. As the most potent known AChE inhibitor, the *syn*1-TZ2PA6 isomer was recently shown to have higher affinity as a reversible organic inhibitor of acetylcholinesterase1 (AChE1) than the *anti*1-TZ2PA6 isomer. Opposite selectivity has been shown for acetylcholinesterase2 (AChE2). In an attempt to understand the selectivity of the *syn*1-TZ2PA6 and *anti*1-TZ2PA6 isomers for AChE1 and AChE2, six molecular dynamics (MD) simulations were carried out with mouse AChE (mAChE, type of AChE1), Torpedo californica AChE (*Tc*AChE, type of AChE1), and Drosophila melanogaster AChE (*Dm*AChE, type of AChE2) bound with *syn*1-TZ2PA6 and *anti*1-TZ2PA6 isomers. Within the structure of the inhibitor, the 3,8-diamino-6-phenylphenanthridinium subunit and 9-amino-1,2,3,4-tetrahydroacridine subunit, *via* π–π interactions, made more favorable contributions to *syn*1-TZ2PA6 or *anti*1-TZ2PA6 isomer binding in the mAChE/*Tc*AChE enzyme than the 1,2,3-triazole subunit. Compared to AChE1, the triazole subunit had increased binding energy with AChE2 due to a greater negative charge in the active site. The binding free energy calculated using the MM/PBSA method suggests that selectivity between AChE1 and AChE2 is mainly attributed to decreased binding affinity for the inhibitor.

1. Introduction

The serine hydrolase acetylcholinesterase (AChE, EC 3.1.1.7) participates in nerve signal transmission in the cholinergic nervous system by hydrolyzing the neurotransmitter acetylcholine. AChE has very high catalytic efficiency, with a turnover of 10^3–10^4 s^{-1}, and operates at a speed near the limit of diffusion [1]. The AChE active site is divided into several subsites, including the catalytic triad, oxyanion hole, anionic subsite, acyl binding pocket, and peripheral anionic site (PAS site). In general, the catalytic triad and anionic subsite (CAS site) are located at the bottom of a deep and narrow groove (~20 Å deep), and the PAS subsite is at the entrance of the active site pocket [2–6]. In recent decades, numerous studies have focused on insect AChE because the enzyme is the target of organophosphates (OP) and carbamates (CB), two important classes of insecticides used in agriculture and public health for pest management [7].

AChE is encoded by the acetylcholinesterase gene (*ace*) and the first invertebrate *ace* gene was cloned in *Drosophila melanogaster*. More than one *ace* gene encodes the synaptic AChE target. Only one AChE gene (now called *ace*2) exists in all true flies (or Cyclorrhapha), a large monophyletic group of the Diptera including the *D. melanogaster*, *Musca domestica*, *Lucilia cuprina*, and *Bactrocera oleae* species. [8] In contrast, many other insects and ticks, such as *Anopheles gambiae* and *Culex pipiens* [9], *Culex tritaeniorhynchus* [10], *Anopheles albimanus* [11], *Boophilus microplus* [12], *Aphis gossypii* [13,14], *Myzus persicae* [15], *Schizaphis graminum* [16], *Plutella xylostella* [17], and *Helicoverpa assulta* [18], have at least two genes encoding AChE, termed *ace*1 and *ace*2. Studies have shown that the *ace*1 played a key role in insecticide toxicology. However, because some insecticides also target *ace*2 [19], a complete understanding of the mechanisms underlying inhibitors selectivity for AChE1 and AChE2 is important.

To date, over 100 crystal structures have been determined for AChE1 (encoded by *ace*1) from *Torpedo californica* (*Tc*AChE) [2] *Electrophorus electicus* (*Ee*AChE) [20] mice (mAChE), and human (hAChE) [5]. However, only three crystal structures have been determined for AChE2 (encoded by *ace*2) [6], all from *D. melanogaster* (*Dm*AChE). Recently, Wiesner et al. [21] found that the three dimensional (3D) structures of AChEs are evolutionarily conserved, despite the difference in their amino acid sequences. Protein folding was also found to be very similar when the structures of hAChE and *Dm*AChE were compared. However, Sussman et al. [22] found that the active-site gorge of *Dm*AChE is significantly narrower than that of *Tc*AChE. In 2002, Lewis et al. [23] synthesized two regioisomers of triazole derivatives, *anti1*-TZ2PA6 and

* Corresponding author at: College of Chemistry, Central China Normal University, Luoyu Road 152, Wuhan 430079, PR China. Tel.: +86 27 67867800; fax: +86 27 67867141.
E-mail address: gfyang@mail.ccnu.edu.cn (G.-F. Yang).

1093-3263/$ – see front matter © 2013 Elsevier Inc. All rights reserved.
http://dx.doi.org/10.1016/j.jmgm.2013.01.004

Table 1
Binding free energies (kcal mol^{-1}) of AChEs proteins complex with *syn*1 and *anti*1-TZ2PA6.

Complex	ΔE_{elc}	ΔE_{vdw}	ΔG_{SA}	ΔG_{PB}	ΔE_{bind}	$-T\Delta S$	ΔG_{bind}	ΔG_{exp} [a]	K_i (fM)[b]
mAChE-*syn*1	−515.31 (6.23)[c]	−85.40 (2.95)	−8.56 (0.09)	549.97 (7.20)	−59.31 (5.33)	24.13 (1.70)	−35.18	−29.53	410
*Tc*AChE-*syn*1	−537.97 (7.20)	−83.83 (2.80)	−7.83 (0.10)	566.33 (7.23)	−63.30 (4.88)	23.65 (1.62)	−39.65	−31.81	77
*Dm*AChE-*syn*1	−710.50 (6.94)	−84.29 (2.41)	−8.24 (0.07)	743.89 (7.21)	−59.14 (4.55)	28.57 (2.37)	−30.57	−26.56	3600
mAChE-*anti*1	−500.31 (5.55)	−87.84 (2.95)	−7.70 (0.07)	537.22 (5.26)	−58.63 (4.11)	32.69 (2.29)	−25.94	−25.31	8900
*Tc*AChE-*anti*1	−538.30 (6.90)	−81.12 (2.89)	−7.79 (0.09)	566.45 (6.09)	−60.76 (4.11)	28.37 (2.77)	−32.39	−28.76	720
*Dm*AChE-*anti*1	−708.41 (7.55)	−85.10 (2.74)	−8.13 (0.08)	741.35 (7.05)	−60.30 (4.25)	29.22 (3.47)	−31.08	−27.58	1700

[a] $\Delta G_{exp} = -RT \ln K_i$.
[b] Ref. [27].
[c] The values in square brackets are the standard error of the calculation.

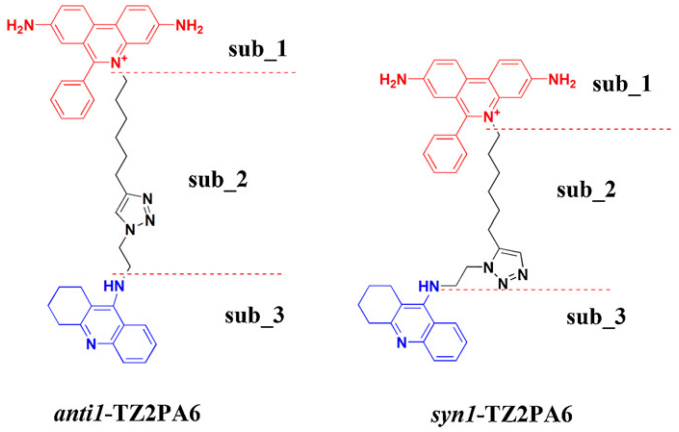

Fig. 1. Chemical structures of *anti1*- and *syn1*-TZ2PA6. The dashed lines indicate the structural subunits of the inhibitors that were investigated in this work, *i.e.*, sub_1 (3,8-diamino-6-phenylphenanthridinium unit), sub_2 (1,2,3-triazole unit), and sub_3 (9-amino-1,2,3,4-tetrahydroacridine unit).

syn1-TZ2PA6 (Fig. 1); the *syn1*-triazole isomer inhibited AChE with an association rate constant near the diffusion limit. Interestingly, the *syn1*-triazole isomer has approximately 9–22 times higher affinity for AChE1 (mAChE and *Tc*AChE) than the *anti1*-triazole isomer, but its binding affinity for AChE2 (*Dm*AChE) is roughly 2-times lower than that of the *anti1*-triazole isomer (Table 1). However, the detailed mechanisms controlling the binding selectivity of these two inhibitors remain unclear.

In the present study, we used various computational techniques, including molecular docking, molecular dynamics (MD), and molecular mechanics-Poisson–Boltzmann surface area (MM/PBSA) calculations [24–26], to investigate the mechanism underlying inhibitor binding that confers selectivity between AChE1 and AChE2, specifically mAChE, *Tc*AChE, and *Dm*AChE. The relative trend of the calculated and experimental binding free energies (ΔG_{bind} and ΔG_{exp}) for the binding of two inhibitors, *anti*1-TZ2PA6 and *syn*1-TZ2PA6, to different targets were compared in order to obtain reasonable binding structures. The computational results reveal that the interactions of inhibitors with PAS and CAS contribute to the binding free energies, but the interactions of inhibitors with PAS significantly contribute to the selectivity. In addition, the area between the PAS and CAS interaction with the linker favorably contributes to selectivity. These findings will provide useful information for designing better selective AChE1/AChE2 inhibitors.

2. Computational methods

2.1. Initial structures

The crystal complex structures of mAChE-*syn*1 and mAChE-*anti*1 (PDB ID codes: 1Q83 and 1Q84, respectively) [27] were used as initial structures for the mAChE systems. As for *Tc*AChE systems, we found that the 2CKM and 2CMF [28] structures of *Tc*AChE overlaid well with 1Q83 and 1Q84, respectively, using the align model in the PYMOL program. Then, the complex structures of *Tc*AChE-*syn*1 and *Tc*AChE-*anti*1 were obtained by directly merging the *syn*1- and *anti*1-TZ2PA6 isomers from 1Q83 and 1Q84 to 2CKM and 2CMF, respectively. Based on the superimposition to the mAChE systems, the 1QON [6] structure was selected for *Dm*AChE. Due to low sequence identity (39%) between mAChE and *Dm*AChE, as obtained from ClustalW2-mutiple sequence alignment (http://www.ebi.ac.uk/Tools/msa/clustalw2, Supporting information), the AutoDock 4 program was employed to perform an efficient docking to gain the *Dm*AChE-*syn*1 and *Dm*AChE-*anti*1 complexes. The active site was defined using Autogrid, and the grid size was set to 50 Å × 50 Å × 50 Å points with 0.375 Å grid spacing centered on the ligand's center of mass. The Lamarckian Genetic Algorithm (LGA) [29] was employed as a search engine. Step size of 0.2 Å for translation and 5.0° for rotation were chosen. The number of individuals in the population was set to 150, a maximum number of energy evaluations were set to 25,000,000 and a maximum number of 27,000 LGA operations were performed. Operator weights for mutation and crossover were set to 0.02 and 0.80, respectively. For each docking simulation, 100 different poses were generated and the poses for molecular dynamics simulation were chosen based on both binding model by visual inspection and estimated binding energy obtained from the AutoDock 4 program.

For crystal structures, all protein bound sugars, all polyethyleneglycols, and other crystallographic agents were deleted. Additionally, the original ligands for 2CKM, 2CMF, and 1QON were removed from the complexes. The missing atoms were added using DiscoverStudio 2.5. A total of six systems, including mAChE, *Tc*AChE, and *Dm*AChE in complex with *syn*1 and *anti*1-TZ2PA6, respectively, were subjected to molecular dynamics simulations.

2.2. Molecular dynamics (MD) simulations

The geometry optimization and electrostatic potential calculations of ligands were calculated at the HF/6-31G* level using the Gaussian03 program [30], and RESP partial charges [31] were assigned using the ANTECHAMBER module of the AMBER8 package. As demonstrated by Antosiewicz et al. [32] the nitrogen atom in the tacrine moiety was protonated for both of ligands. Then all the ligand-protein complexes were neutralized by adding Na^+, and the systems were solvated in an octahedron box of TIP3P [33] water molecules with a minimum solute wall distance of 9 Å. The system contains about 49,000 atoms.

The molecular dynamics simulations were performed using the Sander module of AMBER8 with Amber ff99 force field [34,35] for amino acid residues and General Amber force field for ligands. A residue-based cutoff of 10 Å was utilized for noncovalent interactions. The two stages for energy minimization included first fixing the protein with the harmonic constraint of 100 kcal mol^{-1} Å^{-2},

minimizing the water molecules and Na^+ ions, and then followed by fixing the backbone atoms of the protein with the same strength as mentioned above, and minimizing the sidechains, ligand, water molecules, and Na^+ ions. In these two steps, energy minimization was first performed for 1000 steps by the steepest descent method and 2000 steps by the conjugated gradient method. The SHAKE [36] algorithm was employed to fix all covalent bonds containing hydrogen atoms and the time step for molecular dynamics simulation was set to 2.0 fs. After that, all the systems were gradually heated from $T = 10$ K to $T = 298.15$ K for 10 ps, then equilibrated for 30 ps, and 100 kcal mol^{-1} $Å^{-2}$ harmonic constraint was set for both backbone and ligands before the equilibration simulations. Finally, the MD simulations were performed for 5.5 ns at 1 atm and 298.15 K. During this process, the time step was set to 2.0 fs, and coordinates were collected every 1 ps.

Because of the flexibility of the acyl loop and the omega loop which surrounded the entrance of the active site, all the backbone atoms of the protein were put on 100 kcal mol^{-1} $Å^{-2}$ harmonic constraint to avoiding unreasonable conformation change, otherwise, the large conformation change would take place in the PAS and CAS site. One hundred snapshots of the simulated structure within the last 100 ps stable MD trajectory were selected and minimized to perform the MM/PBSA calculations (see below).

2.3. Binding free energy calculation (MM/PBSA)

The binding free energies were calculated by using the MM-PBSA free energy calculation method. In this method, the binding free energy of the protein-ligand complex (ΔG_{bind}) is obtained from the difference between the free energies of the protein-ligand complex (ΔG_{cpx}) and the unbound receptor (ΔG_{rec}) and the free ligand (ΔG_{lig}) as follows:

$$\Delta G_{bind} = \Delta G_{cpx} - \Delta G_{rec} - \Delta G_{lig} \quad (1)$$

The binding free energy (ΔG_{bind}) can be evaluated as the sum of the changes in the molecular mechanical (MM) gas-phase binding energy (ΔE_{MM}), solvation free energy (ΔG_{sol}), and entropic contribution ($-T\Delta S$). The ΔE_{MM} was evaluated as a sum of electrostatic energy (ΔE_{ele}) and van der Waals interaction energy (ΔE_{vdw}).

$$\Delta G_{bind} = \Delta E_{MM} + \Delta G_{sol} - T\Delta S \quad (2)$$

$$\Delta E_{MM} = \Delta E_{ele} + \Delta E_{vdw} \quad (3)$$

The solvation free energy ΔG_{sol} was composed of two parts:

$$\Delta G_{sol} = \Delta G_{PB} + \Delta G_{np} \quad (4)$$

$$\Delta G_{np} = \gamma SASA + \beta \quad (5)$$

The electrostatic contribution to the solvation free energy (ΔG_{PB}) is evaluated by Poisson–Boltzmann (PB) methods. The nonpolar solvation energy, ΔG_{np}, can be estimated by an empirical relation of $\Delta G_{np} = \gamma SASA + \beta$, where SASA [37,38] and is defined as the solvent-accessible surface area, and the solvation parameters γ and β were set to 0.00542 kcal mol^{-1} $Å^{-2}$ and 0.92 kcal mol^{-1}, respectively. The dielectric constant for the molecule and surrounding solvent were set to 1 and 80, and the probe radius of the solvent was set to 1.4 Å.

Further, the entropy contribution to the binding free energy can be divided into two parts: the solvation free entropy (ΔS_{solv}) and the conformational free entropy (ΔS_{conf}).

$$\Delta S = \Delta S_{solv} + \Delta S_{conf} \quad (6)$$

The solvation free entropy is gained by the tendency of water molecules to minimize their contacts with hydrophobic groups in protein. The conformational free entropy is related to the change of the number of rotatable bonds during the binding process. The detailed computational procedure used to evaluate the entropy contribution ($-T\Delta S$) to the binding free energy was the same as that described in our recent publications [39,40].

3. Results and discussion

3.1. 3D Structures of AChE

Among the subsites of the active pocket of AChE, CAS and PAS are the most important. OP and CB inhibitors always bind at the CAS site, whereas 'divalent' ligands can bind to the CAS and PAS simultaneously. Before MD simulation, we systematically compared the 3D structures of mAChE, *Tc*AChE, and *Dm*AChE (Fig. 2). Although their overall structures were similar (as shown in Fig. S1 in supporting information), they still displayed some differences, especially in the loops. For example, the acyl loop and omega loop respectively contained residues 285–295 (11 residues) and 69–84 (16 residues) of mAChE, residues 278–288 (11 residues) and 66–81 (16 residues) of *Tc*AChE, and residues 320–328 (9 residues) and 67–82 (16 residues) of *Dm*AChE. The omega loop showed only slight variations. The maximum distances between the acyl loop and omega loop were approximately 22.8 Å for mAChE, 23.2 Å for *Tc*AChE, and 18.0 Å for *Dm*AChE. Compared to mAChE and *Tc*AChE, *Dm*AChE lacked two residues in the acyl loop, which led to a large deviation, resulting in a closer proximity of the acyl and omega loops. Subsequently, the entrance to the active site of *Dm*AChE is smaller than that of mAChE and *Tc*AChE. The Tyr71 side chain in *Dm*AChE (corresponding to Asp74 in mAChE and Asp72 in *Tc*AChE) points toward the active site groove. In addition, more negative charges are present in the active site of *Dm*AChE than in the active sites of mAChE and *Tc*AChE. In order to examine the effects of these differences, AChEs in complex with *syn*1/*anti*1-TZ2PA6 were subjected to the following MD simulations.

3.2. Binding energy calculations

At first, MD simulations without any restraint were performed. However, the simulation results showed that the PAS site and CAS site underwent significant structural changes during the simulation. The π–π stacking interaction between the inhibitor and

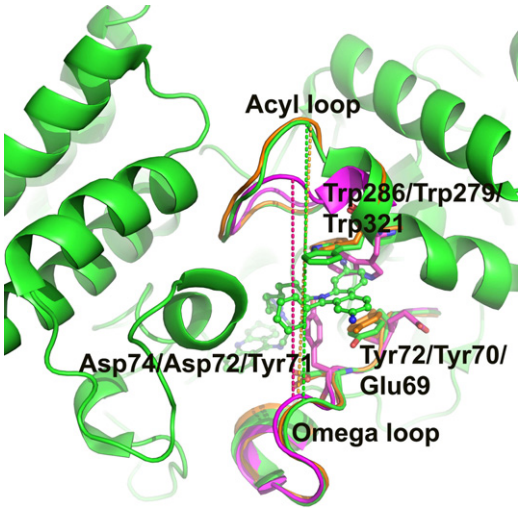

Fig. 2. The top view of the overlay between m/*Tc*/*Dm*AChEs. For clarity, only the full structure of mAChE is shown. The mAChE, *Tc*AChE, and *Dm*AChE are shown in green, orange, and magenta, respectively. The numbering of the residues, in turn, refers to mAChE, *Tc*AChE, and *Dm*AChE. The distances between the acyl and the omega loops, indicated by the green line (mAChE), the orange line (*Tc*AChE), and the magenta line (*Dm*AChE), are 22.8 Å, 23.2 Å, and 18.0 Å, respectively.

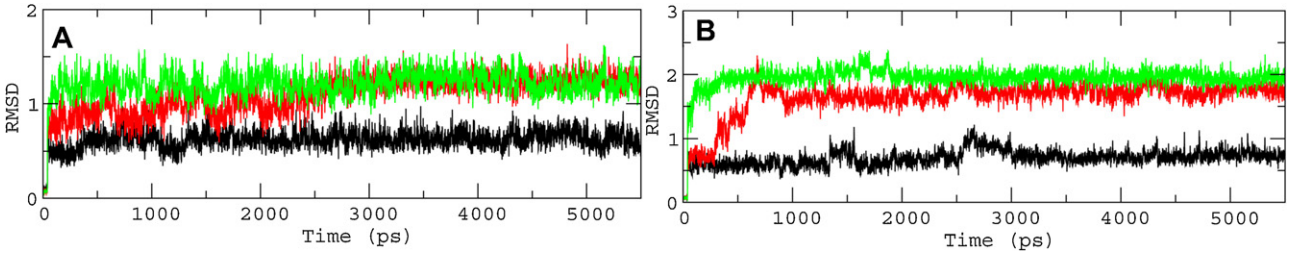

Fig. 3. Plots of RMSD of heavy atoms of *syn*1-TZ2PA6 (A) and *anti*1-TZ2PA6 (B). The black, red and green line represents ligand complexed with mAChE, *Tc*AChE and *Dm*AChE, respectively.

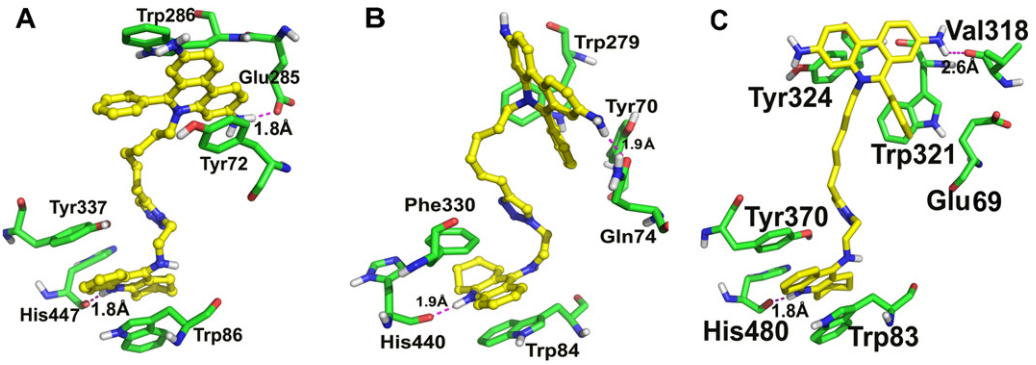

Fig. 4. The average structures of mAChE-*syn*1 (A), *Tc*AChE-*syn*1(B), and *Dm*AChE-*syn*1(C) complexes. The *syn*1-TZ2PA6 is shown as a stick_ball model in yellow and the residues in the protein are shown as stick models in green. The dashed magenta lines represent the H-bonds between residues-ligand. (For interpretation of the references to color in this figure legend, the reader is referred to the web version of this article.)

residues Trp286/279/321 in m/*Tc*/*Dm*AChE made a significant contribution to the binding, but it disappeared during the simulations. Therefore, considering the flexibility of the acyl loop and the omega loop and keeping the stability of the whole structure, the backbone atoms of protein were fixed during the MD simulation.

The energy components, temperature, and volume were found to be reasonably stable throughout the 5.5 ns simulation (data not shown), indicating that the system reached equilibrium. Due to the restraint of the backbone atoms of the enzymes during MD simulations, the RMSD values for the heavy atoms for the ligand during the production phase relative to the starting structures were determined and are provided in Fig. 3. During the MD simulations, all of the systems achieved equilibrium quickly. The average RMSD values were 0.61 ± 0.09, 1.24 ± 0.08, and 1.22 ± 0.1 Å for the mAChE-*syn*1, *Tc*AChE-*syn*1, and *Dm*AChE-*syn*1 complexes, respectively, and 0.75 ± 0.07, 1.78 ± 0.07, and 1.94 ± 0.09 Å for the mAChE-*anti*1, *Tc*AChE-*anti*1, and *Dm*AChE-*anti*1 complexes, respectively. Compared to the *Dm*AChE and *Tc*AChE systems, the RMSD values of the mAChE systems were smaller. We also noted that the RMSD values of the AChEs in complex with *syn*1-TZ2PA6 were smaller than those of the AChEs in complex with *anti*1-TZ2PA6. In addition, we compared the initial structures of the mAChE-*syn*1 and mAChE-*anti*1 complexes with the average structures obtained in MD simulations (Figs. S2 and S3 in the supporting information), which further confirmed the stability of the MD binding models of mAChE in complex with *syn*1-TZ2PA6 and *anti*1-TZ2PA6.

The ΔE_{bind} (binding energy neglecting the contribution of entropy) calculated for all protein-ligand complexes ranged from -58.63 to -63.30 kcal mol^{-1}; *syn*1-TZ2PA6 had the most negative ΔE_{bind} value (-63.30 kcal mol^{-1}) and the highest activity toward *Tc*AChE, and *anti*1-TZ2PA6 had the least negative ΔE_{bind} value (-58.63 kcal mol^{-1}) and the lowest activity toward *m*AChE. Interestingly, the most and least favorable ΔG_{bind} calculated from the MD simulations also referred to *Tc*AChE-*syn*1 (-39.65 kcal mol^{-1}) and *Tc*AChE-*anti*1 (-25.94 kcal mol^{-1}). A good linear correlation ($r^2 = 0.96$) existed between the calculated ΔG_{bind} value and ΔG_{exp} ($\Delta G_{exp} = -RT \ln K_i$), suggesting that the AChE selectivity is mainly attributed to the decrease in binding affinity for the inhibitor.

3.3. Structures of AChEs-syn1 complexes

Average structures were produced for the AChE-*syn*1 complexes by superimposing the enzyme conformations onto the initial structure and then determining the mean atom positions (Fig. 4). We identified both similarities and differences between the AChE-*syn*1 complexes. To identify the contribution of the separate structural units of the ligands to the binding free energy (Fig. 1), the ligands were split into three subunits: the 3,8-diamino-6-phenylphenanthridinium unit (sub_1), 1,2,3-triazole unit (sub_2), and 9-amino-1,2,3,4-tetrahydroacridine unit (sub_3). Similar to the

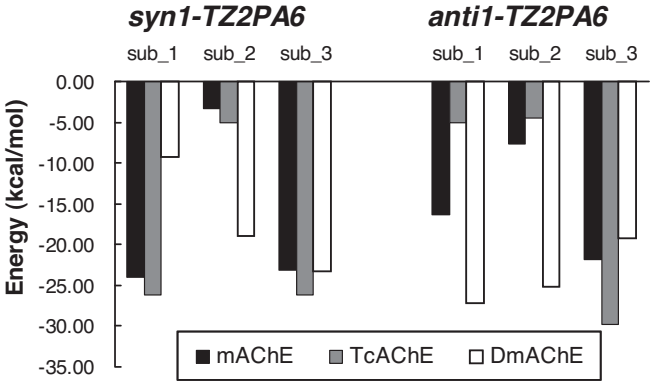

Fig. 5. Comparison of the binding energy between the subunits of *syn*1- and *anti*1-TZ2PA6 with AChEs.

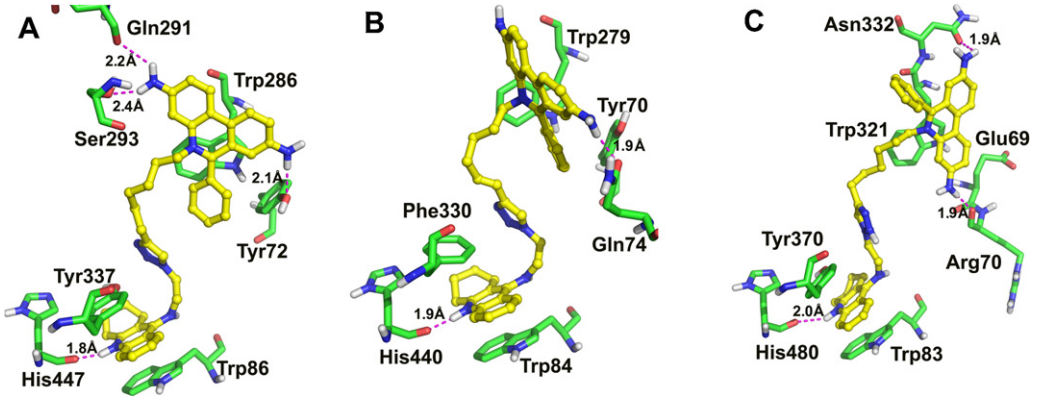

Fig. 6. The average structures of mAChE-*anti*1 (A), *Tc*AChE-*anti*1 (B), and *Dm*AChE-*anti*1 (C) complexes. The *anti*1-TZ2PA6 is shown as a stick_ball model in yellow and the residues in the protein are shown in a stick model in green. The dashed magenta lines represent the H-bonds between residues-ligand.

binging free energy calculation, the binding energies of each subunit with the protein were calculated based on the last 100 ps by using the MM/PBSA method. As a general trend, the sub_1 and sub_3 units made more favorable contributions than the sub_2 unit, *via* π–π interactions in the mAChE-*syn*1 and *Tc*AChE-*syn*1 complexes (Fig. 5). However, the *Dm*AChE-syn1 complex gave the opposite result.

In Fig. 4, the sub_1 unit of *syn*1-TZ2PA6 adopted distinct orientations in the PAS sites of the three complexes; sub_1 was sandwiched by Trp286 and Tyr72 in mAChE and Trp279 and Tyr70 in *Tc*AChE. In the *Dm*AChE-*syn*1 complex, Glu69 replaced the Tyr72 of mAChE and Tyr70 of *Tc*AChE. The π–π interaction between sub_1 and Glu69 disappeared, and the phenyl group in *syn*1-TZ2PA6 exhibited only a *T*–π interaction (meaning the two rings are perpendicular to each other) with Trp321 in *Dm*AChE. In addition, sub_1 formed a H-bonds with Glu285 in mAChE (1.8 Å) and Glu278 in *Tc*AChE (1.7 Å). This H-bond disappeared in *Dm*AChE, but a new H-bond formed with Val318 with a distance of 2.6 Å (Fig. 4C). As a result, the binding energy of sub_1 for *Dm*AChE suffered a loss of approximately 15 kcal mol^{-1}, providing a reasonable explanation for why *Dm*AChE showed the lowest sensitivity to *syn*1-TZ2PA6.

The tacrine moiety (sub_3 unit) of *syn*1-TZ2PA6 displayed almost the same binding model in the CAS site, forming π–π stacking interactions with Trp86 and Try337 in *m*AChE-*syn*1, Trp84 and Phe330 in *Tc*AChE-*syn*1, and Trp83 and Tyr370 in *Dm*AChE-*syn*1, and H-bond interactions with His447 in *m*AChE (1.8 Å), His440 in *Tc*AChE (2.0 Å), and His480 (1.8 Å) in *Dm*AChE. Compared to the corresponding binding energies of the mAChE-*syn*1 and *Dm*AChE-*syn*1 complexes, both sub_1 and sub_3 in the *Tc*AChE-*syn*1 complex exhibited higher binding energies, which accounted for the greater inhibition of *Tc*AChE by *syn*1-TZ2PA6.

3.4. Structures of AChEs-anti1 complexes

Average structures were obtained for the AChE-*anti*1 complexes using MD simulations as shown in Fig. 6. Similar to the AChE-*syn*1 complexes, sub_3 in the AChE-*anti*1 complexes also formed π–π stacking with Tyr337 and Trp86 in mAChE, Phe330 and Trp84 in *Tc*AChE, and Tyr370 and Trp83 in *Dm*AChE. In addition, similar H-bond interactions were observed with His447 in *m*AChE, His440 in *Tc*AChE, and His480 in *Dm*AChE. As shown in Fig. 5, sub_3 of *anti*1-TZ2PA6 exhibited stronger affinity for *Tc*AChE than for *m*AChE and *Dm*AChE, which accounts for the higher inhibitory effects of *anti*1-TZ2PA6 against *Tc*AChE.

In contrast, sub_1 of *anti*1-TZ2PA6 had different binding modes at the PAS site. In the mAChE-*anti*1 complex (Fig. 6A), sub_1 of *anti*1-TZ2PA6 interacted with Trp286 and Tyr72 *via* π–π and *T*–π stacking and formed two H-bonds with Gln291 and Ser293. For the *Tc*AChE-*anti*1 complex, sub_1 of *anti*1-TZ2PA6 did not form π–π interactions with any residues in the PAS site, and it only formed a single H-bond with Gln74 (Fig. 6B), and it formed a π–π interaction with Trp321 and two H-bonds with Arg70 and Asn332 in the *Dm*AChE-*anti*1 complex (Fig. 6C). Because the active site of *Dm*AChE has a stronger negative charge than the active site of mAChE and *Tc*AChE, the sub_1 and sub_2 units extending over the groove of the AChE active site make greater contributions to the binding affinity than sub_3. As a result, *anti*1-TZ2PA6 was a stronger inhibitor against *Dm*AChE than mAChE.

4. Conclusion

Through extensive computational simulations, our investigations elucidated the selectivity mechanism of AChE inhibitors. Binding energy analysis of different subunits of *syn*1-TZ2PA6 and *anti*1-TZ2PA6 isomers revealed that the sub_1 and/or sub_3 units are the main contributors to binding affinity, whereas the sub_2 unit exhibited significant differences in binding affinity for the three different types of AChEs. According to the mechanism discovered herein, several aspects should be considered in the design of selective AChE inhibitors. The structure of an inhibitor should consist of three parts: (1) a positively charged aromatic ring to bind the PAS site, (2) an aromatic ring to bind the CAS site, and (3) a linker. Inhibitor selectivity between AChE1 and AChE2 can be achieved by modifying the structure of the positively charged aromatic ring and/or linker. For AChE1, the inhibitor should contain a larger positively charged aromatic ring, such as 3,8-diamino-6-phenylphenanthridinium, to match the shape and properties of the PAS. In addition, a wider linker, such as 1,2,3-triazole, would also improve selectivity.

Acknowledgments

The research was supported in part by the National Basic Research Program of China (No. 2010CB126103), the NSFC (No. 20902034, 20925206 and 20932005) and the National Key Technologies R&D Program (2011BAE06B05).

Appendix A. Supplementary data

Supplementary data associated with this article can be found, in the online version, at http://dx.doi.org/10.1016/j.jmgm.2013.01.004.

References

[1] T.L. Rosenberry, Acetylcholinesterase, Advances in Enzymology and Related Areas of Molecular Biology 43 (1975) 103–218.

[2] J.L. Sussman, M. Harel, F. Frolow, C. Oefner, A. Gpldman, L. Toker, I. Silman, Atomic structure of acetylcholinesterase from *Torpedo californica*: a prototypic acetylcholine-binding protein, Science 253 (1991) 872–879.

[3] Y. Bourne, Z. Radic, G. Sulzenbacher, E. Kim, P. Taylor, P. Marchot, Substrate, Product trafficking through the active center gorge of acetylcholinesterase analyzed by crystallography and equilibrium binding, Journal of Biological Chemistry 281 (2006) 29256–29267.

[4] J.P. Colletier, D. Bourgeois, B. Sanson, D. Fournier, J.L. Sussman, I. Silman, M. Weik, Shoot-and-trap: use of specific X-ray damage to study structural protein dynamics by temperature-controlled cryo-crystallography, Proceedings of the National Academy of Sciences of the United States of America 105 (2008) 11742–11747.

[5] G. Kryger, M. Harel, K. Giles, L. Toker, B. Velan, A. Lazar, C. Kronman, D. Barak, N. Ariel, A. Shafferman, I. Silman, J.L. Sussman, Structures of recombinant native and E202Q mutant human acetylcholinesterase complexed with the snake-venom toxin fasciculin-II, Acta Crystallographica. Section D: Biological Crystallography 56 (2000) 1385–1394.

[6] M. Harel, G. Kryger, T.L. Rosenberry, W.D. Mallender, T. Lewis, R.J. Fletcher, J.M. Guss, I. Silman, J.L. Sussman, Three-dimensional structures of *Drosophila melanogaster* acetylcholinesterase and of its complexes with two potent inhibitors, Protein Science 9 (2000) 1063–1072.

[7] J.I. Kim, C.S. Jung, Y.H. Koh, S.H. Lee, Molecular, biochemical and histochemical characterization of two acetylcholinesterase cDNAs from the German cockroach *Blattella germanica*, Insect Molecular Biology 15 (2006) 513–522.

[8] E. Huchard, M. Martinez, H. Alout, E.J. Douzery, G. Lutfalla, A. Berthomieu, C. Berticat, M. Raymond, M. Weill, Acetylcholinesterase genes within the Diptera: takeover and loss in true flies, Proceedings of the Royal Society – Biological Sciences 273 (2006) 2595–2604.

[9] M. Weill, P. Fort, A. Berthomieu, M.P. Dubois, N. Pasteur, M. Raymond, A novel acetylcholinesterase gene in mosquitoes codes for the insecticide target and is nonhomologous to the ace gene Drosophila, Proceedings of the Royal Society of London B 269 (2002) 2007–2016.

[10] T. Nabeshima, A. Mori, T. Kozaki, Y. Iwata, O. Hidoh, S. Harada, S. Kasai, D.W. Severson, Y. Kono, T. Tomita, An amino acid substitution attributable to insecticide insensitivity of acetylcholinesterase in a Japanese encephalitis vector mosquito, *Culex tritaeniorhynchus*, Biochemical and Biophysical Research Communications 13 (2004) 794–801.

[11] R.H. Ffrench-Constant, B.C. Bonning, Rapid microtitre plate test distinguishes insecticide resistant acetylcholinesterase genotypes in the mosquitoes *Anopheles albimanus*, *A. nigerrimus* and *Culex pipiens*, Medical and Veterinary Entomology 3 (1989) 9–16.

[12] G.D. Baxter, S.C. Barker, Analysis of the sequence and expression of a second putative acetylcholinesterase cDNA from organophosphate-susceptible and organophosphate-resistant cattle ticks, Insect Biochemistry and Molecular Biology 32 (2002) 815–820.

[13] J. Benting, R. Nauen, Biochemical evidence that an S431F mutation in acetylcholinesterase-1 of *Aphis gossypii* mediates resistance to pirimicarb and omethoate, Pest Management Science 60 (2004) 1051–1055.

[14] S. Toda, S. Komazaki, T. Tomita, Y. Kono, Two amino acid substitutions in acetylcholinesterase associated with pirimicarb and organophosphorous insecticide resistance in the cotton aphid, *Aphis gossypii* Glover (Homoptera: Aphididae), Insect Molecular Biology 13 (2004) 549–553.

[15] T. Nabeshima, T. Kozaki, T. Tomita, Y. Kono, An amino acid substitution on the second acetylcholinesterase in the pirimicarb-resistant strains of the peach potato aphid, *Myzus persicae*, Biochemical and Biophysical Research Communications 307 (2003) 15–22.

[16] J.R. Gao, S. Kambhampati, K.Y. Zhu, Molecular cloning and characterization of a greenbug (*Schizaphis graminum*) cDNA encoding acetylcholinesterase possibly evolved from a duplicate gene lineage, Insect Biochemistry and Molecular Biology 32 (2002) 765–775.

[17] J.H. Baek, J.I. Kim, D.W. Lee, B.K. Chung, T. Miyata, S.H. Lee, Identification and characterization of ace1-type acetylcholinesterase likely associated with organophosphate resistance in *Plutella xylostella*, Pesticide Biochemistry and Physiology 81 (2005) 164–175.

[18] D.W. Lee, S.S. Kim, S.W. Shin, W.T. Kim, K.S. Boo, Molecular characterization of two acetylcholinesterase genes from the oriental tobacco budworm, *Helicoverpa assulta* (Guenee), Biochimica et Biophysica Acta 1760 (2006) 125–133.

[19] M. Alon, F. Alon, R. Nauen, S. Morin, Organophosphates' resistance in the B-biotype of *Bemisia tabaci* (Hemiptera: Aleyrodidae) is associated with a point mutation in an ace1-type acetylcholinesterase and overexpression of carboxylesterase, Insect Biochemistry and Molecular Biology 38 (2008) 940–949.

[20] Y. Bourne, J. Grassi, P.E. Bougis, P. Marchot, Conformational flexibility of the acetylcholinesterase tetramer suggested by X-ray crystallography, Journal of Biological Chemistry 274 (1999) 30370–30376.

[21] J. Wiesner, Z. Kriz, K. Kuca, D. Jun, J. Koca, Acetylcholinesterases-the structural similarities and differences, Journal of Enzyme Inhibition and Medicinal Chemistry 22 (2007) 417–424.

[22] I. Silman, J.L. Sussman, Acetylcholinesterase: how is structure related to function, Chemico-Biological Interactions 175 (2008) 3–10.

[23] W.G. Lewis, L.G. Green, F. Grynszpan, Z. Radić, P.R. Carlier, P. Taylor, M.G. Finn, K.B. Sharpless, Click chemistry in situ: acetylcholinesterase as a reaction vessel for the selective assembly of a femtomolar inhibitor from an array of building blocks, Angewandte Chemie International Edition 41 (2002) 1053–1057.

[24] X.L. Zhu, W.C. Yang, N.X. Yu, S.G. Yang, G.F. Yang, Computational simulations of structural role of the active-site W374C mutation of acetyl-coenzyme-A carboxylase: multi-drug resistance mechanism, Journal of Molecular Modeling 17 (2011) 495–503.

[25] X.L. Zhu, G.F. Hao, C.G. Zhan, G.F. Yang, Computational simulations of the interactions between acetyl-coenzyme-A carboxylase and clodinafop: resistance mechanism due to active and nonactive site mutations, Journal of Chemical Information and Modeling 49 (2009) 1936–1943.

[26] G.F. Hao, X.L. Zhu, F.Q. Ji, L. Zhang, G.F. Yang, C.G. Zhan, Understanding mechanism of drug resistance due to a codon deletion in protoporphrinogen oxidase through computational modeling, Journal of Physical Chemistry B 113 (2009) 4865–4875.

[27] Y. Bourne, H.C. Kolb, Z. Radic, K.B. Sharpless, P. Taylor, P. Marchot, Freeze-frame inhibitor captures acetylcholinesterase in a unique conformation, Proceedings of the National Academy of Sciences of the United States of America 101 (2004) 1449–1454.

[28] E.H. Rydberg, B. Brumshtein, H.M. Greenblatt, D.M. Wong, D. Shaya, L.D. Williams, P.R. Carlier, Y.P. Pang, I. Silman, J.L. Sussman, Complexes of alkylene-linked tacrine dimers with *Torpedo californica* acetylcholinesterase: binding of Bis5-tacrine produces a dramatic rearrangement in the active-site gorge, Journal of Medicinal Chemistry 49 (2006) 5491–5500.

[29] G.M. Morris, D.S. Goodsell, R.S. Halliday, R. Huey, W.E. Hart, R.K. Belew, A.J. Olson, Automated docking using a lamarckian genetic algorithm and an empirical binding free energy function, Journal of Computational Chemistry 19 (1998) 1639–1662.

[30] M.J. Frisch, G.W. Trucks, H.B. Schlegel, G.E. Scuseria, M.A. Robb, J.R. Cheeseman, J.A. Montgomery Jr., T. Verven, K.N. Kudin, J.C. Burant, J.M. Millam, S.S. Iyengar, J. Tomasi, V. Barone, B. Mennucci, M. Cossi, G. Scalmani, N. Rega, G.A. Petersson, H. Nakatsuji, M. Hada, M. Ehara, K. Toyota, R. Fukuda, J. Hasegawa, M. Ishida, T. Nakajima, Y. Honda, O. Kitao, H. Nakai, M. Klene, X. Li, J.E. Knox, H.P. Hratchian, J.B. Cross, C. Adamo, J. Jaramillo, R. Gomperts, R.E. Stratmann, O. Yazyev, A.J. Austin, R. Cammi, C. Pomelli, J.W. Ochterski, P.Y. Ayala, K. Morokumo, G.A. Voth, P. Salvador, J.J. Dannenberg, V.G. Zakrzewski, S. Dapprich, A.D. Daniels, M.C. Strain, O. Farkas, D.K. Malick, A.D. Rabuck, K. Raghavachari, J.B. Foresman, J.V. Ortiz, Q. Cui, A.G. Baboul, S. Clifford, J. Cioslowski, B.B. Stefanov, G. Liu, A. Liashenko, P. Piskorz, I. Komaromi, R.L. Martin, D.J. Fox, T. Keith, M.A. Al-Laham, C.Y. Peng, A. Nanayakkara, M. Challacombe, P.M. Gill, M.W. Wong, C. Gonzalez, J.A. Pople, Gaussian 03, Revision A.1, Gaussian, Inc., Pittsburgh, 2003.

[31] W.D. Cornell, P. Cieplak, C.I. Bayly, P.A. Kollmann, Application of RESP charges to calculate conformational energies, hydrogen bond energies, and free energies of solvation, Journal of the American Chemical Society 115 (1993) 9620–9631.

[32] J. Antosiewicz, S.T. Wlodek, J.A. McCammon, Acetylcholinesterase: role of the enzyme's charge distribution in steering charged ligands toward the active site, Biopolymers 39 (1996) 85–94.

[33] W.L. Jorgensen, J. Chandrasekhar, J.D. Madura, Comparison of simple potential functions for simulating liquid water, Journal of Chemical Physics 79 (1983) 926–935.

[34] V. Hornak, R. Abel, A. Okur, B. Strockbine, A. Roitberg, C. Simmerling, Comparison of multiple Amber force fields and development of improved protein backbone parameters, Proteins 65 (2006) 712–725.

[35] D.A. Case, T. Darden, T.E. Cheatham III, C. Simmerling, J. Wang, R.E. Duke, R. Luo, AMBER8 Users' Manual, University of California, 2004.

[36] J.P. Ryckaert, G. Ciccotti, H.J.C. Berendsen, Numerical integration of the cartesian equations of motion of a system with constraints: molecular dynamics of n-alkanes, Journal of Computational Physics 23 (1977) 327–341.

[37] D. Sitkoff, K.A. Sharp, B. Honig, Accurate calculation of hydration free energies using macroscopic solvent models, Journal of Physical Chemistry 98 (1994) 1978–1988.

[38] M.L. Connolly, Analytical molecular surface calculation, Journal of Applied Crystallography 16 (1983) 548–558.

[39] F.Q. Ji, C.W. Niu, C.N. Chen, Q. Chen, G.F. Yang, Z. Xi, C.G. Zhan, Computational design and discovery of conformationally flexible inhibitors of acetohydroxyacid synthase to overcome drug resistance associated with the W586L mutation, ChemMedChem 3 (2008) 1203–1206.

[40] Y.M. Pan, D.Q. Gao, C.G. Zhan, Modeling the catalysis of anti-cocaine catalytic antibody: competing reaction pathways and free energy barriers, Journal of the American Chemical Society 130 (2008) 5140–5149.